Title

Progressive Changes in Liquefaction and Cone Penetration Resistance across Multiple Shaking Events in Centrifuge Tests

Journal

Journal of Geotechnical and Geoenvironmental Engineering, 145(3)

ISSN

1090-0241

Authors

Darby, Kathleen M
Boulanger, Ross W
DeJong, Jason T
et al.

Publication Date

2019-03-01

DOI

10.1061/(asce)gt.1943-5606.0001995

Peer reviewed

Progressive changes in liquefaction and cone penetration resistance across multiple shaking events in centrifuge tests

Kathleen M. Darby, S.M.ASCE (Corresponding author)
Graduate Student Researcher, Department of Civil and Environmental Engineering, University of California at Davis, Davis, CA 95616. E-mail: kdarby@ucdavis.edu

Ross W. Boulanger, F.ASCE
Professor, Department of Civil and Environmental Engineering, University of California at Davis, Davis, CA 95616. E-mail: rwboulanger@ucdavis.edu

Jason T. DeJong, M.ASCE
Professor, Department of Civil and Environmental Engineering, University of California at Davis, Davis, CA 95616. E-mail: jdejong@ucdavis.edu

Jaclyn D. Bronner
Staff Geotechnical Engineer, GeoEngineers, Inc., Redmond, WA 98052: E-mail: jbronner@geoengineers.com

Author's version in April 2018 prior to copyediting, final edits,
and publication in the JGGE

ABSTRACT

The effects of shaking history on CPT based liquefaction triggering correlations for clean saturated sand are examined using cone penetration resistance and cyclic strength data pairs from dynamic centrifuge model tests. Three model tests on a 9-m radius centrifuge examine liquefaction responses of level profiles of saturated Ottawa F-65 sand subjected to multiple (17 to 29) shaking events that produced successive changes in density and model response characteristics. Inverse analysis of data from dense accelerometer arrays are used to define time series of cyclic stress ratios and shear strains throughout the profile. Cyclic resistance ratios against triggering of ~100% excess pore pressure ratio in 15 equivalent uniform cycles are computed at multiple depths based on weighting of the cyclic stress ratio time series up to the time of triggering. Cone penetration tests performed at select times during each model test are used to define the variation in cone tip resistances with depth and shaking history. The resulting data pairs, with normalized cone tip resistances ranging from 20 to 340 and cyclic resistance ratios ranging from 0.1 to 2.0, show that both quantities progressively increase as a result of recurrent liquefaction events, and generally follow the trends predicted by case history based liquefaction triggering correlations. Three 1-m radius centrifuge tests of similar configurations produced consistent results. Implications for the interpretation of case histories and engineering practice are discussed.

INTRODUCTION

Various liquefaction triggering correlations have been developed based on data obtained from case histories. In these correlations, some in-situ measurement of soil strength or stiffness [typically standard penetration test (SPT), cone penetration test (CPT), or shear wave velocity (V_s)] is paired with an estimate of the cyclic stresses imposed on the soil during earthquake loading. Data pairs are classified as either liquefaction or non-liquefaction events based on surficial observations of damage (or lack thereof) associated with liquefaction, such as ground cracking, sand boils, settlement, or lateral deformations. While case histories are essential for developing or validating liquefaction triggering correlations, there are significant uncertainties in the interpretation of many case histories and critical data gaps in the case history databases. For example, many case histories only have post-earthquake site investigation (CPT, SPT, V_s) data; the effects of prior shaking events on penetration resistances (q_c) or shear wave velocity (V_s) have not been well quantified, resulting in uncertainty as to the magnitude of any bias that might be introduced to the correlations by using uncorrected post-event investigation data. Additionally, consensus has not been reached on the influence of prior shaking events on a soil's liquefaction resistance. The 2010-11 Canterbury, NZ earthquake sequence demonstrated the ability of a site to liquefy during multiple sequential events (van Ballegooy et al. 2014); however, these events occurred over a relatively short time frame, such that the observed responses may not be representative of behaviors across shaking events separated by greater periods of time.

Efforts have also been made to develop CPT-based liquefaction triggering correlations from experimental data and analytical studies. For example, Mitchell and Tseng (1990) combined cone penetration resistances predicted by cavity expansion analyses with cyclic stress ratios measured by laboratory testing for four clean sands. Carraro et al. (2003) developed triggering relationships

for clean and silty sands by similarly combining cone penetration analyses with cyclic triaxial test data. Kokusho et al. (2012) directly developed triggering correlations for sand with varying fines content by preparing specimens in a cyclic triaxial apparatus and performing mini cone penetrometer tests in the specimens before they were cyclically loaded.

The effects of cyclic loading on cyclic strength have been examined in a number of laboratory studies. Finn et al. (1970) found the effect of strain history on liquefaction resistance of sand to be dependent on the magnitude of applied strain and pore pressure generated during pre-straining cycles. Oda et al. (2001) observed similar results and suggested the development of fabric anisotropy to be a significant factor. Singh et al. (1982) and Goto and Nishio (1988) compared the results of cyclic triaxial tests conducted on loose (D_R=48%) and dense (D_R=90%) sands with and without strain history and found an increase in cyclic resistance following prior strain cycles. Shaking table tests on saturated sands by Ha et al. (2011) showed an initial decrease in the liquefaction resistance, followed by an increase in liquefaction resistance (indicated by excess pore pressure generation) after multiple liquefaction events. Cyclic direct simple shear (DSS) tests involving repeated shearing and reconsolidation phases, beginning with normally consolidated specimens, showed progressive increases in cyclic strength of Ottawa F-65 sand (Parra Bastidas et al. 2016) and non- and low plasticity silt (Price et al. 2017), whereas tests on initially over-consolidated specimens showed that liquefaction could reduce the cyclic strength for a subsequent loading stage. These and other laboratory studies provide a level of control on loading history that is not possible with case history field data, but evaluating their implications for practice requires estimating how loading history also affects cone penetration resistance or other in-situ test measurements.

Recent studies have used shaking table and centrifuge tests to examine the relative effects of cyclic loading on D_R, V_s, q_c, and liquefaction resistance. Centrifuge tests conducted by El-Sekelly et al. (2015, 2016) on saturated silty sand models found D_R increased by 38-50% and V_s increased by less than 10% after being subjected to low to mid-level pre-shaking events. Liquefaction resistance (measured by excess pore pressure generation) was found to increase overall following pre-shaking, though stronger pre-shaking events were found to temporarily decrease liquefaction resistance. Additional tests conducted by El-Sekelly et al. (2017) on Ottawa sand attributed this loss of liquefaction resistance following a stronger shaking event to a loss in lateral stress (K_o) during liquefaction. Stronger subsequent events were observed to cumulatively increase D_R up to 58% and non-uniformly increase V_S up to 20%, as compared to the initial value, and erase the liquefaction resistance developed during pre-shaking. A large scale shaking table test conducted as part of the same study found q_c to be more sensitive to shaking history compared to V_s (Dobry et al. 2016). Darby et al. (2016) conducted a set of 1-m radius dynamic centrifuge tests using mini cone penetration tests to investigate the simultaneous effects of multiple shaking events on the cyclic resistance ratio (CRR) and q_c within the same saturated Ottawa sand models; results indicate q_c increases due to shaking events, but that the relationship between CRR and q_c seems to be minimally affected by shaking history.

This paper presents an evaluation of the effects of shaking history on CPT based liquefaction triggering correlations for clean saturated sand using cone penetration resistance and cyclic strength data pairs from dynamic centrifuge model tests. Three model tests on a 9-m radius centrifuge examine liquefaction responses of level profiles of saturated Ottawa sand subjected to multiple (17 to 29) shaking events that produced successive changes in density and model response. Inverse analysis of data from dense accelerometer arrays are used to define time series

of cyclic stress ratios (CSRs) and shear strains throughout the profile. The time series of accelerations, pore pressures (from matching arrays of pore pressure transducers), CSRs, and shear strains are used to identify those depth intervals where liquefaction responses are relatively well-defined compared to depth intervals where liquefaction responses vary strongly with depth or time (e.g., large gradients in strain or pore pressure versus depth or variations in CSR across short time intervals). Cyclic resistance ratios (CRRs) against triggering for approximately 100% excess pore pressure ratio in 15 equivalent uniform cycles are computed at multiple depths based on weighting of the CSR time series up to the time of triggering. Cone penetration tests performed at select times during each model test are used to define the variation in cone tip resistances ($q_{cN} = q_c/P_a$, where P_a = atmospheric pressure) with depth and shaking history. The compiled set of CRR and q_{cN} values, along with the adjustments described later in this paper, are tabulated in the electronic supplement. The resulting data pairs, with q_{cN} ranging from 20 to 340 and CRRs ranging from 0.1 to 2.0, were binned into categories of high, medium, and low confidence based on criteria regarding various sources of experimental uncertainty. The derived data show that both CRR and q_{cN} progressively increase as a result of prior shaking and recurrent liquefaction events, and generally follow the trends predicted by case history based liquefaction triggering correlations. In addition, the post-triggering response (peak shear strains and surface settlements) tended to decrease as the model progressively densified, although the trends are moderated by the fact that site response effects, such as amplification, became stronger as the soils became denser. These results are augmented with a set of results from three 1-m radius centrifuge tests of similar configurations; these models had limited instrumentation and thus have limitations in their interpretations. Specific shaking events in the large and small centrifuge tests illustrate some additional observations, including: effect of centrifuge spin-down/spin-up on soil response, the

potential for reduced cyclic strength immediately following a strong shaking event, and the complex variation in behaviors observed throughout a soil profile during earthquake shaking. The implications of these results for the interpretation of case histories and engineering practice are discussed.

Centrifuge Models

Three centrifuge models with level saturated sand profiles were constructed in a flexible shear beam container and tested at the UC Davis Center for Geotechnical Modeling using the 9-m radius centrifuge. All tests were performed at a centrifugal acceleration of 40-g; results are reported in prototype scale using standard dynamic scaling laws unless otherwise noted. Each model consisted of approximately 245-273 mm (model scale) of Ottawa F-65 sand overlying 180 mm (model scale) of Monterey sand. Representative plan and cross-sectional views are presented in Figure 1 (sections with model specific dimensions are included in the electronic supplement). In two of the models, the Ottawa sand layer was placed loose, at initial $D_{Ro} \approx 43\%$ (Model 1) and $\approx 25\%$ (Model 2). In the third model, the Ottawa sand layer was placed dense, at an initial $D_{Ro} \approx 80\%$ (Model 3). For all three models, the underlying Monterey sand was placed dense, at an initial $D_{Ro} \approx 85\%$. Models were constructed in a series of lifts, using dry pluviation from constant drop heights. Lift thicknesses ranged from 40 mm (model scale) (Ottawa sand) to 60 mm (model scale) (Monterrey sand). Fully constructed models were saturated bottom-up under vacuum with a solution of methycellulose and water prepared to a viscosity of 20 cS (model scale). Increasing the pore fluid viscosity at 1-g counteracts the decrease in diffusion time at 40-g; ideally pore fluid viscosity would equal the testing g-level, but practical constraints arise from saturating at 1-g limits the maximum practical viscosity (Stewart et al. 1998).

Each model was instrumented with dense vertical arrays of pore pressure transducers (PPTs), accelerometers (ACCs) and linear potentiometers (LPs) to measure the dynamic response of the soil during shaking. Locations of sensors are shown in the plan and cross-sectional views in Figure 1. Settlement measured at the locations of the arrays at 1-g at select times during the testing sequence was found to be consistent with settlements measured by LPs. Sensor depths vary throughout the shaking sequence as the soils undergo volumetric strains and settle; these changes in position are approximately tracked based on the measured settlements and inverse analysis results. Two vertical arrays of PPTs and ACCs were placed in each model for a total of 17 PPTs and 22 ACCs per model.

Each model was subjected to multiple shaking events, each consisting of fifteen uniform cycles of sinusoidal base acceleration at a frequency of 1.0 Hz. The 1.0 Hz input frequency was selected to be below the natural frequency of the Ottawa sand layer in both the non-liquefied and liquefied condition. Motions were applied at the base in the longitudinal (referred to as north-south) direction. Peak base accelerations (PBAs) were progressively increased from about 0.03g in shaking event 1 to 0.25g in shaking event 6. This shaking sequence was repeated several times during each test. Achieved PBAs varied slightly between models and shaking events due to equipment limitations. Additionally, near the end of testing, models were subjected to a stronger motion with PBA = 0.30g (Model 1), 0.55g (Model 2), or 0.40g (Model 3).. The excess pore pressure ratio (r_u), which is the ratio of excess pore pressure (u_e) to initial vertical effective stress (σ'_{vo}), was calculated at each PPT depth during each shaking event. The PBA and peak r_u for Model 1 are plotted versus shaking event number (29 shaking events total) in Figure 2. Symbols are plotted versus PBA on the left y-axis, with symbol shape representing the sensor depth (2.7 m, 4.1 m, or 5.4 m) and symbol color representing the magnitude of peak r_u (red indicates $r_u \geq 0.95$,

yellow indicates peak r_u between 0.70-0.95, and white indicates peak $r_u < 0.70$). Actual sensor depths varied throughout testing (due to settlement of the sensors and/or surrounding soil); average depths are reported in figures containing data from multiple events. Average volumetric strain, which is estimated as the measured surface settlement divided by the thickness of the Ottawa sand layer, is depicted in grey and plotted on the right y-axis. The PBA, peak r_u, and average volumetric strain during each shaking event in Models 2 (with 26 shaking events) & 3 (with 17 shaking events) are provided in Figures 3 & 4, respectively, using the same format. For all models, a wait time of approximately 15 min (in model scale) was maintained between shaking events, which was several times greater than the time required for full dissipation of any measured excess pore pressures.

A 6 mm (model scale) diameter cone penetrometer pushed at 10 mm/s was used to measure changes in penetration resistance at select times during each test; the timing of each sounding is indicated by the blue arrows along the top of Figures 2-4. The cone diameter is 30 times the Ottawa sand's median particle size of 0.20 mm, which exceeds the cone to particle size ratio of 20 that Bolton et al. (1999) found necessary to avoid particle size effects. Eight cones were pushed in the initially loose models (Models 1 & 2) and eleven cones were pushed in the initially dense model (Model 3). In Model 1, one cone was pushed before any shaking events (cone 1), two after each of the 6^{th} (cones 2 & 3) and 12^{th} shaking events (cones 4 & 5), and one after the 19^{th} (cone 6), 25^{th} (cone 7), and 28^{th} shaking events (cone 8). In Model 2, one cone was pushed before any shaking events (cone 1), two after the 6^{th} (cones 2 & 3), 12^{th} (cones 4 & 5), and 18^{th} (cones 6 & 7) shaking events, and one after the 24^{th} shaking event (cone 8). In Model 3, four cones were pushed before any shaking (cones 1-4), two after the 6^{th} shaking event (cones 5 & 6), one after the 12^{th} (cone 7), 13^{th} (cone 8), and 16^{th} shaking events (cone 9), and two after the final 17^{th} shaking event (cones 10 & 11). Cones obtained after shaking events were pushed at the end of the 15 min wait period.

Details regarding the cone testing procedures and interpretation can be found in Darby et al. (2017).

Calculation of Cyclic Shear Stress and Shear Strain Time Series

Shear stress and shear strain time series were computed using the filtered acceleration data and inverse one-dimensional site response analysis methods outlined in Kamai and Boulanger (2010) and Brandenberg et al. (2010). Inverse analyses of acceleration data have been shown to be reliable when the wavelength is eight times greater than the sensor spacing. With an input frequency of 1 Hz and minimum sensor spacing of 1.2 m, the analyses should be reasonable for shear wave velocities as low as 10 m/s, which is lower than the wave speeds observed even after liquefaction for these models. Acceleration data were filtered using a 4^{th} order Butterworth bandpass filter with corner frequencies of 0.33 and 60 Hz; corner frequencies were selected based on sensor limitations and previous centrifuge experience. Shear stress time series at the mid-point between ACCs are computed from the filtered acceleration data using a mass-weighting procedure (Kamai et al. 2010). Shear stress time series are converted to cyclic stress ratio (CSR) time series by dividing by σ'_{vo}. Shear strain time series are computed by double integrating filtered acceleration data with respect to time, followed by differentiating with respect to depth using the method of weighted residuals outlined in Brandenberg et al. (2010).

Typical Dynamic Responses

The responses from four different shaking events in Model 1 are used to illustrate typical responses across the range of those observed, and are shown in Figures 5-8. Shear strain and acceleration time series at select depths are shown in the left panel, and excess pore pressure and CSR time series at matching depths are shown in the right panel. The bottom graph in both panels plots the base acceleration, while the top graphs in these panels plot the shear strain and CSR at the

shallowest depth. The far right columns indicate the depth of each measurement and the CRR category (discussed later). In the right panel of time series, stars indicate the time at which r_u first reaches 0.95; dashed arrows project these times onto adjacent CSR time series. The triggering of $r_u \approx 1.0$ was identified using a calculated $r_u \geq 0.95$ to account for the small experimental uncertainties with which excess pore pressure and initial vertical effective stress at each transducer location can be determined. Responses are shown for the 4th, 10th, 12th, and 29th shaking events in Model 1; similar figures for dynamic responses in Model 3 are provided in the supplement.

The response of Model 1 during the 4th shaking event (PBA ≈ 0.11g), shown in Figure 5, illustrates the effects of liquefaction on a loose model. During this event, $r_u \geq 0.95$ was generated at a depth of 3.5 m in only one or two cycles of loading, whereas r_u=0.95 was not reached until approximately seven to ten cycles of loading at depths of 5.0 m and 6.5 m; r_u=0.95 was not reached at a depth of 2.0 m. Triggering of liquefaction coincided with a strong drop in accelerations and CSRs in the upper half of the Ottawa sand layer. The observation that $r_u \geq 0.95$ was not reached at 2.0 m depth is attributed to the drop in loading (CSR) at this depth due to liquefaction/softening of the underlying layers. However, the trend of excess pore pressure generation at a depth of 2.0 m suggests that $r_u \geq 0.95$ would have been expected with additional stronger loading cycles, with the approximate time indicated by the green circle. Peak shear strains in the 3-6 m depth interval were approximately 2.0-2.5%, with the deeper layers experiencing less shear strain compared to the shallower layers. In general, shear strains were largest (about 2%) near the time of liquefaction triggering, after which they oscillated at a value approximately 0.5% lower than the peak strain. This reduction in shear strains after liquefaction was triggered in the mid portion of the Ottawa sand layer is attributed to the change in site response characteristics and the associated reduction in CSRs. The measured and computed responses at both arrays (solid lines for array 1 and dashed

lines for array 2) were similar at all depths. Sensor depths in the two arrays varied slightly due to differences in movement during shaking, saturation, and construction.

The response of Model 1 during the 10th shaking event (PBA ≈ 0.12g), shown in Figure 6, illustrates how the dynamic response changed as a result of several prior liquefaction events (six of the prior nine shaking events induced liquefaction at some depth; Figure 2). Figure 6 shows the same measurements as those indicated in Figure 5, although the depths have changed slightly due to settlement during the intermediate shaking events. The PBA during shaking event 10 is similar to the PBA during the previously shown 4th shaking event (Figure 5), but the dynamic response is significantly different. During shaking event 10, $r_u \geq 0.95$ was reached at depths of 2.2, 3.6, and 4.8 m, but was not reached at depths of 6.5 m and deeper. The triggering of $r_u \geq 0.95$ occurred earlier at the shallow depths (2-3 loading cycles) and later at the deeper depths (10-11 loading cycles). The triggering of $r_u \geq 0.95$ at each depth coincided with the onset of strong acceleration spikes at those depths, indicative of a stronger cyclic mobility response than was observed in shaking event 4. Peak shear strains exceeded 3% at depths of 0.4 to 0.5 m early in shaking, whereas peak shear strains reached about 1.5% at depths of 2.6 to 4.2 m later in shaking. The measured accelerations in the two arrays show significant differences near the soil surface, which results in computed CSRs that also differ significantly near the surface. The dynamic response after liquefaction triggering in shaking event 10, compared to shaking event 4, is consistent with the expected effects of increased relative density.

The response of Model 1 during the 12th shaking event (PBA ≈ 0.21g), shown in Figure 7, illustrates the response under a stronger shaking event (i.e., PBA is 75% greater than for shaking event 10 in Figure 6). Significant pore pressure is generated at all depths early in shaking; $r_u \geq 0.95$ develops after half a loading cycle at shallow depths and after 2-3 loading cycles at deeper depths.

The acceleration spikes that developed after triggering of $r_u \geq 0.95$ were stronger, often exceeding 1g. The magnitude of these acceleration spikes after triggering of $r_u \geq 0.95$ increased over the duration of shaking at a depth of 6.5 m, but decreased over the shaking duration at a depth of 2.2 m. Peak shear strains exceeded 4% at depths of 0.4 to 0.5m and ranged from 2-3% throughout the rest of the layer.

The response of Model 1 during the 29th shaking event (PBA ≈ 0.29g), shown in Figure 8, illustrates that it no longer triggers $r_u \geq 0.95$ at any depth at the strongest shaking level after the model has been sufficiently densified. Accelerations are amplified up through the soil profile, reaching peaks of 0.7-0.8g near the soil surface. Peak r_u of up to 0.60 developed in the upper portion of the Ottawa sand. Shear strains as large as 1% developed at depths of 2.5 m or less, but were closer to 0.5% at larger depths. The absence of liquefaction triggering despite CSRs well in excess of 1.0 illustrates the dramatic increase in cyclic strength caused by this sequence of shaking events.

Calculation of CRRs Against Triggering of $r_u \approx 1.00$

Determining CRRs against triggering of ru=1.00 required three primary steps: (1) converting irregular CSR time series to uniform CSR time series, (2) identifying the time of triggering to convert CSR to CRR values, and (3) adjusting CRRs to a common overburden stress and accounting for bi-directional shaking to facilitate comparisons to case history based correlations. This section addresses each of these steps.

Converting irregular CSR times series to uniform CSR time series

The irregular CSR time series for each depth interval and shaking event are converted to equivalent uniform CSR time series for different time intervals, including: the full time series, the time up to the triggering of $r_u \geq 0.95$, and other windows for sensitivity analysis. The conversion of an

irregular time series to an equivalent uniform time series is performed following the fatigue-based procedure described in Seed et al. (1975). This procedure assumes the relationship between the CRR and number of cycles to cause failure (N) has the form:

$$CRR = a \cdot N^{-b} \quad (1)$$

This relationship is used to convert each half cycle of the irregular loading history to a specified reference CSR. For example, a half cycle at CSR_B corresponds to the following equivalent number of cycles at a reference CSR_A:

$$N_A = \left(\frac{CSR_B}{CSR_A}\right)^{1/b} (1/2\ cycle) \quad (2)$$

Half cycles of loading were defined by a reversal across zero shear stress. The conversion process was performed in two steps. First, the total number of equivalent cycles was determined for a reference CSR equal to the maximum CSR from the irregular time series. Second, that result was converted to the equivalent uniform CSR corresponding to 15 uniform loading cycles (i.e., CSR_{15cyc}). Parra Bastidas et al. (2016) reported b-values of 0.15 and 0.17 for Ottawa sand at $D_R \approx$ 40% and 80%, respectively, in cyclic direct simple shear (DSS) tests. Ziotopoulou and Morales (2018) report a larger b-value of 0.24 for Ottawa sand at $D_R \approx 64\%$, also in cyclic DSS tests. Both of these studies used specimens prepared by air pluviation, consistent with the centrifuge model preparation method. For the present study, the conversion process was performed using a baseline b-value of 0.20, followed by sensitivity analyses using values of 0.16 and 0.24. Alternative weighting schemes (e.g., Green and Terri 2005) would also affect the results of this conversion process, although this aspect is not examined herein.

Defining CRR values for different depth intervals

CRR values were determined from the CSR loading up to the time of triggering $r_u \geq 0.95$, with the time of triggering determined from the PPTs immediately above and below the depth at which

the CSR was computed. For example, consider the CSR time series at 5.9 m depth in Figure 5 (shaking event 4); the time to trigger is 15 s at 4.8 m depth (array 1), 17.8 s at 5.1 m depth (array 2), 16.8 s at 6.3 m depth (array 1), and 15.6 s at 6.6 m depth (array 2). These four different triggering times are used to compute equivalent CRR_{15cyc} values from the CSR time series for each of the accelerometer arrays, resulting in a total of four CRR_{15cyc} estimates. These four CRR_{15cyc} estimates ranged from 0.090 to 0.098, with an average of 0.094. This average value represents the properties at this depth with a relatively high degree of confidence, given the well-defined triggering time, similarity of pore pressure responses above and below the location of stress calculation, and similarity of responses in both arrays.

In some situations, the estimated CRR_{15cyc} values are sensitive to the vertical and lateral (between array) variations in the measured pore pressure and acceleration responses. For example, the triggering time associated with the CSR time series at 2.7 m depth in Model 1 during shaking event 10 (Figure 6) ranges from 8.1-8.5 s at 2.2 m depth (just above the CSR depth) to 15.7 s at 3.6 m depth (just below the CSR depth). The computed CRR_{15cyc} varies from 0.225 (at array 1) to 0.301 (at array 2), for a 29% difference in average CRR_{15cyc} between the two arrays; with the difference in triggering times being the primary cause for variations in CRR_{15cyc}. For another example, the triggering time associated with the CSR time series at 4.2 m depth in this same shaking event ranges from 15.7 s at 3.6 m depth (above the CSR depth) to 15.3-16.7 s at 4.8 m depth (below the CSR depth); this range in triggering times is not large, but it spans one half cycle of loading within which the CSR spiked (due to the acceleration spikes), such that the CRR_{15cyc} estimates ranged from 0.191 to 0.241, with a 37% range within array 1. For these two examples, there is a relatively low degree of confidence that these estimated CRR_{15cyc} values represent the

soil properties at these depths, given their sensitivity to the identified triggering times and differences in array responses.

In other situations, estimating CRR_{15cyc} can be complicated by differences in excess pore pressure generation behavior above and below the depth at which the CSR is calculated. For example, the CSR times series at 5.5 m depth in Model 1 during shaking event 10 (Figure 6) becomes spiky near 16 s which suggests that liquefaction has been triggered. The PPTs at 4.8 m depth (above the CSR depth) indicate triggering of $r_u \geq 0.95$ at 15.3 to 16.7 s, whereas the PPTs at 6.5 m depth (below the CSR depth) indicate r_u values only reaching 0.75-0.85 at the end of shaking (21.0 s). Assuming that liquefaction was triggered at the CSR depth sometime between 15.3 s and 21.0 s, the estimated CRR_{15cyc} values agree within 9% from the average. In this case, there is a medium degree of confidence in the estimated CRR_{15cyc} value given the absence of triggering immediately below the CSR depth.

The CRR_{15cyc} results were binned into high-, medium-, and low-confidence categories based on the criteria listed in Table 1. High confidence CRR_{15cyc} values correspond to depths where liquefaction was triggered at the PPTs above and below the depth of interest, and the computed CRR values are relatively insensitive to temporal and spatial (vertical and lateral) variations in the pore pressure and acceleration responses. Medium confidence CRR_{15cyc} values meet the same criteria as high confidence values, except that $r_u \geq 0.95$ may not have been triggered either above or below the depth of interest. Low confidence CRR_{15cyc} values do not meet the criteria for high or medium confidence values, but still correspond to points where $r_u \geq 0.95$ was triggered either at the PPTs above or below the depth of interest.

In addition, equivalent CSR values for 15 uniform cycles of loading (CSR_{15cyc}) were determined for each entire CSR time series. These values describe the loading for non-triggering

cases (no triggering above or below the depth of interest) as well as for loading after triggering, as discussed later.

Adjusting CRRs to a reference overburden stress and bidirectional loading conditions

The CSR_{15cyc} and CRR_{15cyc} values from each depth interval were adjusted to the same reference overburden stress since cyclic strength and penetration resistance are known to depend on overburden stress. Various liquefaction triggering procedures use an overburden stress of 1 atm (101 kPa) as the reference stress, although this is purely for convenience and they can be algebraically translated to any other reference stress. The adjustment of the CSR_{15cyc} and CRR_{15cyc} for 1 atm overburden stress was performed using the following relationships by Boulanger and Idriss (2004):

$$K_\sigma = 1 - C_\sigma \ln\left(\frac{\sigma'_{vc}}{P_a}\right) \leq 1.1 \quad (3)$$

$$C_\sigma = \frac{1}{18.9 - 17.3 D_R} \leq 0.3 \quad (4)$$

The adjustments of CSR_{15cyc} and CRR_{15cyc} values to σ'_{vc} = 1 atm ranged between 3-9% because the overburden stresses ranged from 25-75 kPa for the depths of interest.

The $CSR_{15cyc,\sigma'=1}$ and $CRR_{15cyc,\sigma'=1}$ values from each depth interval were then reduced by 10% to account for expected differences between the 1-D shear loading in the centrifuge and the 2-D horizontal loading that develops in the field (Pyke et al. 1974, Seed 1979, Ishihara 1996).

Cone Penetration Resistances

Cone penetration profiles were obtained at the times shown in Figures 2, 3, and 4 for Models 1, 2, and 3, respectively. Profiles of q_c in Model 1 are shown in Figure 9a; similar results were obtained in Models 2 and 3, and were presented in Darby et al. (2017). The cone penetration resistances were adjusted to the reference overburden stress of 101 kPa using the following equations:

$$q_{c1N} = \left(\frac{q_c}{Pa}\right)\left(\frac{Pa}{\sigma'_{vc}}\right)^m \quad (5)$$

$$m = 0.784 - 0.521 * D_R \quad (6)$$

$$D_R = 0.465\left(\frac{q_{c1N}}{C_1}\right)^{0.264} - C_2 \quad (7)$$

Equation (7) is a modified form of the q_{c1N}-D_R relationship presented in Idriss and Boulanger (2008) with constants C_1 and C_2 calibrated for Ottawa sand. C_1 and C_2 were calibrated based on initial cone data from the three centrifuge tests described herein, and are estimated to be 3.09 and 0.514, respectively (see Darby et al. 2017 for details). The cone penetration resistances are significantly influenced by boundaries within a distance of 5 to 10 cone diameters; data from within 5 cone diameters of the soil surface or underlying Monterey sand interface are not used when calculating representative penetration resistances or relative densities. Additionally, representative penetration resistances for a specific depth are taken as the average over a 5 cone diameter thick zone centered about the depth of interest.

The progressive increase in penetration resistances with each shaking event for Model 1 is shown in Figures 9a and 9b, with the corresponding estimates for D_R shown in Figure 9c. The progressive increases in penetration resistance and D_R were not uniform throughout the profile, with densification generally occurring earlier in the shaking sequence and reaching larger values at the bottom of the profile and occurring later in the shaking sequence and reaching smaller values near the top of the profile.. This non-uniform densification can be partially attributed to upward drainage during and after shaking, as discussed in greater detail in Darby et al. (2017). Similar trends were observed for Models 2 and 3.

Representative penetration resistances for different depths and shaking events were obtained by linearly interpolating between measured penetration resistances based on measured surface settlements. This interpolation procedure is illustrated in Figure 10 for the middle of the Ottawa

sand layer for Model 1. Measured penetration resistances (red diamonds) are plotted versus the cumulative surface settlement up to the time of each cone penetration test. The cone penetration resistance prior to each of the shaking events (black x marks) is then linearly interpolated between the measured penetration resistances based on the cumulative settlement prior to the shaking event. When two cone penetration tests were separated in time by a spin-down/spin-up sequence without any shaking event (e.g., cones 2 & 3 for Model 1 in Figure 10), the penetration resistance prior to spin-down/spin-up (cone 2) is used to anchor the interpolation for prior events (i.e., between cones 1 & 2) and the penetration resistance after spin-down/spin-up (cone 3) is used to anchor the interpolation for the following events (i.e., between cones 3 & 4). The small reduction in penetration resistance following a spin-down/spin-up sequence is attributed to a reduction in K_o, as discussed in Darby et al. (2017). The same interpolation procedure was used for the other depths at which CSR_{15cyc} and CRR_{15cyc} values were determined.

Correlation of CRR with q_c

The correlation of CRR with q_c was examined by plotting the $CRR_{15cyc,\sigma'=1}$ against the q_{c1N} for the same depth, for each of the shaking events and models. The $CRR_{15cyc,\sigma'=1}$ and q_{c1N} values, and the intermediate steps in their computation, are listed in Tables S1-S6 of the electronic Supplement. These data are limited to three depths, at approximately one-third, mid-, and two-thirds depth in the Ottawa sand layer, that are sufficiently far from the soil surface and Monterey sand layer to be relatively unaffected by those boundaries. The results are plotted in Figure 11a for Models 1 and 2, which were constructed loose and became dense over many shaking events, and in Figure 11b for Model 3, which was constructed dense. The high, medium, and low confidence points correspond to the green diamonds, yellow triangles, and red circles, respectively. The non-liquefaction points are plotted as open circles. Also plotted in both figures are the case history

based correlations by Boulanger & Idriss (2015) for 16, 50, and 84 percent probability of liquefaction based on model uncertainty alone (i.e., conditional on knowing the loading and penetration resistance). The case history based curves are dashed at CRR levels that are greater than covered by the case history database. The high and medium confidence $CRR_{15cyc,\sigma'=1} - q_{c1N}$ pairs are generally consistent with the case history based correlation, though several of the high confidence $CRR_{15cyc,\sigma'=1} - q_{c1N}$ pairs fall below the correlation. The low confidence $CRR_{15cyc,\sigma'=1} - q_{c1N}$ pairs show poorer agreement, but exhibit trends that are consistent with the case history based correlation and generally plot above the 84% probability of liquefaction curve. Non-triggering $CSR_{15cyc,\sigma'=1} - q_{c1N}$ tend to plot below the case history based correlations, with few exceptions. The results from all three model tests indicate that triggering of liquefaction triggering ($r_u \geq 0.95$) was limited to q_{c1N} values less than about 200, with few exceptions as discussed later.

The $CRR_{15cyc,\sigma'=1} - q_{c1N}$ data in Figures 11a and 11b exhibit no apparent bias or trends with regard to depth, triggering time, or model test, although the variability in the data would make it difficult to identify anything but strong effects. The correlation for $CRR_{15cyc,\sigma'=1}$ at q_{c1N} of 140 to 300 appears to be equally applicable for models that became dense through a multitude of shaking events (Models 1 and 2) and the model that was constructed dense (Model 3); this suggests that the cone penetration resistance adequately reflects the combined effects of densification and strain history on cyclic strength, as has been implicitly assumed in most CPT-based liquefaction triggering correlations.

The response of Model 2 to shaking events 25 and 26 (the last two events) and the response of Model 3 to shaking events 13 and 14 illustrate different responses immediately following an extremely strong loading, as shown in Figures 12a and 12b, respectively (note the change in y axis scale relative to earlier figures). Large acceleration spikes occurred in Model 2 during shaking

event 25 and Model 3 during shaking event 13, producing corrected CSRs of 1.5 to 2.1 at different depths. This strong shaking triggered $r_u \geq 0.95$ throughout the Ottawa sand layer in both models. Model 2 was subsequently shaken with a significantly weaker motion, (shaking event 26 with PBA = 0.09g) which still triggered $r_u \geq 0.95$ throughout the Ottawa sand layer, despite the fact that similar shaking levels in prior events (shaking events 15 & 21) had not triggered $r_u \geq 0.95$ for this same model. Model 3 was also subsequently shaken with a weaker motion (shaking event 14 with PBA = 0.13g), but it did not trigger $r_u \geq 0.95$ within the sand profile. The triggering of $r_u \geq 0.95$ in Model 2 during shaking event 26 was accompanied by peak shear strains of 0.5-0.8%, whereas peak shear strains were only 0.1% in Model 3 during event 14. Thus, the extremely strong shaking of event 25 for Model 2 appears to have had a weakening effect on the sand for the subsequent event, whereas the similarly strong shaking in event 13 for Model 3 did not have the same degree of weakening effect. This difference in responses may be due to shaking event 25 for Model 2 being marginally stronger than shaking event 13 for Model 3, the q_{c1N} values being marginally smaller in Model 2 than in Model 3 at the time of these shaking events (q_{c1N} = 160-250 versus 185-262), or the differences in their shaking histories. The potential loss of liquefaction resistance immediately following a strong shaking event is consistent with behavior reported by El Sekelly (2015, 2016) for silty sands, although the present tests involve denser soils and stronger levels of loading.

The results from three similar tests on a 1-m radius centrifuge, as plotted in Figure 13a, are generally consistent with the results obtained from the three large centrifuge tests (results for all three tests combined in Figure 13b). The small centrifuge tests provided an economical means for establishing testing protocols and analysis methods, but the small model size resulted in greater uncertainty in the analysis and interpretation of results. The small model size meant that only 4 to

5 accelerometers or pore pressure transducers could be arranged in a vertical array, which did not provide enough resolution on the distribution of pore pressure ratios or strains versus depth. In addition, the smaller model size meant that a greater portion of the cone penetration profiles were affected by the boundaries (soil surface and container base). Despite these limitations, the data obtained using the small centrifuge are generally consistent with both the large centrifuge data and the case history based correlations. Details of the small centrifuge tests, along with results from the first test, are provided in Darby et al. (2016).

Maximum Shear Strain Responses

The maximum shear strain responses for all three models show a dependence on penetration resistance, the maximum r_u generated, and the intensity of cyclic loading. The maximum shear strain that developed in each shaking event for all three models is plotted versus $CSR_{15cyc,\sigma'=1}$ in Figures 14a and 14b for points with $r_u < 0.95$ and points with $r_u \geq 0.95$, respectively. The q_{c1N} prior to each shaking event is indicated by the symbol coloring and shape, where $q_{c1N} < 85$ are indicated asblue circles, $85 \leq q_{c1N} < 120$ are indicated as red triangles, $120 \leq q_{c1N} < 160$ are indicated as green diamonds, $160 \leq q_{c1N} < 200$ are indicated as yellow squares and $q_{c1N} \geq 200$ are indicated as cyan downward triangles. None of the points from Model 3 fall in the $q_{c1N} < 85$ bin, while only six of the points from Model 2 fall in the $q_{c1N} \geq 200$ bin. The majority of non-triggering points correspond to maximum shear strains less than 1% (with only five exceptions per Figure 14a), whereas the majority of triggering points correspond to maximum shear strains greater than 1% (with seven points exceeding 3% per Figure 14b). For the same $CSR_{15cyc,\sigma'=1}$, the maximum shear strain tends to decrease with increasing q_{c1N} for both the triggered and non-triggered points. For the triggered points (Figure 14b), about half reached their maximum shear strain after triggering

$r_u \geq 0.95$ whereas the other half developed their maximum shear strains prior to triggering $r_u \geq 0.95$.

Discussion

The cone penetration resistance and cyclic resistance ratio for soils in the field are influenced by a number of factors not addressed in this study, including soil age, cementation, fabric, ground motion characteristics (e.g., frequency content, duration), and system response characteristics (e.g., partial drainage). CRR and penetration resistance generally increase with aging (e.g Seed 1979; Mesri et al. 1990). CRR and pore pressure generation are significantly affected by the fabric produced by different sample preparation methods (e.g., Mulilis et al. 1977, Abdoun et al. 2013). Fabric changes during cyclic loading, such as breaking cementation, are not captured in these tests of young, clean sand. The cyclic loading applied in these tests consisted of uniform sine waves; seismic events are non-uniform both in regards to frequency, amplitude, and duration, all of which are expected to influence liquefaction triggering behavior. The measured surface settlements show small amounts of settlement during shaking (i.e., partial drainage), which nonetheless would be expected to contribute to an increase in cyclic strength during shaking. Regardless, the results generally agree with the case history based correlations, which do account for the above phenomena, suggesting that the correlation of CRR with cone penetration resistance is not overly sensitive to these other factors.

The CRR-q_c data generated from these centrifuge tests are influenced by the effects of sensor location uncertainty and pore water flow on the pore pressure ratios. PPTs move during model construction and testing, which affects the calculations of initial vertical effective stress and excess pore pressure. To account for sensor movement, the locations of sensors are measured at model construction and dissection, and apparent depths (relative to the standing water surface) before and

after each shaking event are back-calculated from the measured hydrostatic pore water pressure. Pore water flow patterns can be inferred from the pore pressure isochrones, and the total amount of pore fluid exiting the sand layer during shaking can be assessed based on surface settlement measurements. The total volume of pore fluid exiting during shaking is a small portion of the eventual post-shaking volume changes (settlements), although a quantitative assessment of drainage effects on CRR values requires more detailed analyses than covered herein. After shaking has ended, the rate of water flowing into the upper layer exceeds the rate of water flowing out of the upper layer, which either maintained high excess pore pressures or even increased excess pore pressures in some cases. In some cases, upward pore water flow caused r_u to exceed 0.95 after strong shaking, but these points are not included in the present correlation because they represent a system response rather than a correlation between cone penetration resistance and the CRR for undrained conditions.

Conclusion

Three dynamic centrifuge model tests on a 9-m radius centrifuge were used to examine the progressive changes in cyclic strength and cone penetration resistance for a clean saturated sand over multiple (17 to 29) shaking events. Inverse analyses of the data from dense accelerometer arrays were used to define time series of cyclic stress ratios and shear strains throughout the profile. Cyclic resistance ratios against triggering of approximately 100% excess pore pressure ratio in 15 equivalent uniform cycles were computed at multiple depths based on weighting of the cyclic stress ratio time series up to the time of triggering. Cone penetration tests performed at select times during each model test were used to define the variation in cone tip resistances with depth and shaking history.

The CRR_{15cyc} and q_{cN} values both progressively increased as a result of prior shaking and recurrent liquefaction events, and generally followed the trends of case history based liquefaction triggering correlations (with comparisons shown for the correlation by Boulanger and Idriss 2015). The initially liquefiable sand layer progressively densified more rapidly at the lower depths, such that triggering of liquefaction in later shaking events was often limited to the shallower depths. The determination of CRR_{15cyc} was often complicated by this vertical variation in pore pressures, as well by lateral variations in pore pressures (between arrays) and sensitivity of the CRR_{15cyc} to the identified triggering time if it coincided with the strongest CSR cycles. The $CRR_{15cyc} - q_{cN}$ pairs were subsequently classified as high, medium, or low confidence values depending on sensitivity of the CRR_{15cyc} to these potential sources of error. The $CRR_{15cyc} - q_{cN}$ pairs are in good agreement with case history based correlations for loose to medium-dense conditions, where the CRR_{15cyc} values were more frequently determined with high confidence. The $CRR_{15cyc} - q_{cN}$ pairs for medium-dense to dense conditions were more frequently of lower confidence and exhibited greater scatter relative to the case history based correlation. Nonetheless, the centrifuge data generally confirm for the case history based correlations, including the extrapolation of these relationships to extremely large CRR_{15cyc} values (i.e., in the 1.0 to 2.0 range). In one case, it was observed that triggering of $r_u \geq 0.95$ at extremely large CSR_{15cyc} values when the sand was dense caused a substantial reduction in triggering resistance for a subsequent shaking event, although the maximum shear strains and post-liquefaction reconsolidation strains remained relatively small because the sand was dense. The results from three 1-m radius centrifuge tests of similar configurations were consistent with those from the more detailed 9-m radius centrifuge tests. The overall consistency of these centrifuge test results with the case history based correlation suggests

that a correlation of CRR with cone penetration resistance can reasonably account for variations in both relative density and shaking history for clean, young, non-cemented sands.

The experimental procedures and interpretation techniques developed for this study represent a promising approach for deriving liquefaction triggering correlations for a range of soil types for which case history data are limited.

Acknowledgements

The National Science Foundation (NSF) provided the funding for this research (Grant No. CMMI-1300518) and for the Natural Hazards Engineering Research Infrastructure (NHERI) centrifuge facility at UC Davis (Grant No. CMMI-1520581). The views and conclusions presented in this paper are solely the authors' and do not necessarily reflect the views or opinions of NSF. This research would not have been possible without the help of Mohammad Khosravi, Ali Khosravi, Alex Strum, Kevin Kuei, Matt Burrall, Bao Li Zheng, Sean Munter, Erik Maroney, Diane Moug, and Dan Wilson. The authors would like to thank the staff and researchers at the UC Davis Center for Geotechnical Modeling for their assistance and the University of Western Australia for the CPT design.

Supplemental Data

Tables S1-S6 and Figures S1-6 are available online in the ASCE Library (http://www.ascelibrary.org).

References

Abdoun, T., Gonzalez, M. A., Thevanayagam, S., and Dobry, R. (2013). "Centrifuge and large-scale modeling of seismic pore pressures in sands: Cyclic strain interpretation". *Journal of Geotechnical and Geoenvironmental Engineering*. 10.1061/(ASCE)GT. 1943-5606.0000821, 1215-1234.

Andrus, R. D., and Stokoe, K. H., (2000). “Liquefaction resistance of soils from shear-wave velocity”, *Journal of Geotechnical and Geoenvironmental Engineering.,* ASCE 126(11), 1015-025.

Bolton, M. D., Gui, M. W., Garnier, J., Corte, J. F., Bagge, G., Laue, J. and Renzi, R. (1999). “Centrifuge cone penetration tests in sand”. *Geotechnique* 49(4). 543-552.

Boulanger, R. W. (2003). "High overburden stress effects in liquefaction analyses." *Journal of Geotechnical and Geoenvironmental Engineering*, ASCE, 129(12), 1071-1082.

Boulanger, R. W. and Idriss, I. M., (2004). “State normalization of penetration resistances and the effect of overburden stress on liquefaction resistance”. Proceedings, 11th International Conference on Soil Dynamics and Earthquake Engineering, and 3rd International Conference on Earthquake Geotechnical Engineering, D. Doolin et al., eds., Stallion Press, Vol. 2, pp. 484-91.

Boulanger, R. W., and Idriss, I. M. (2014). “CPT and SPT based liquefaction triggering procedures”. Report No. UCD/CGM-14/01, Center for Geotechnical Modeling, Department of Civil and Environmental Engineering, University of California, Davis, CA.

Boulanger, R. W., and Idriss, I. M. (2015). “CPT-based liquefaction triggering procedure”, *Journal of Geotechnical and Geoenvironmental Engineering,* ASCE 142(2): 04015065, 10.1061/(ASCE)GT.1943-5606.0001388.

Brandenberg, S. J., Wilson, D. W. & Rashid, M. M. (2010). “A weighted residual numerical differentiation algorithm applied to experimental bending moment data”. *Journal of Geotechnical and Geoenvironmental Engineering.* 136(6), 854-863.

Carraro, J. A. H., Bandini, P., and Salgado, R. (2003). "Liquefaction resistance of clean and nonplastic silty sands based on cone penetration resistance". *Journal of Geotechnical and Geoenvironmental Engineering.* 129(11), 965-976.

Darby, K. M., Bronner, J. D., Parra Bastidas, A. M., Boulanger, R. W., and DeJong, J. T. (2016). "Effect of shaking history on cone penetration resistance and cyclic strength of saturated sand". Proceedings, Geotechnical and Structural Engineering Congress, ASCE, Phoenix, AZ, February 14-17.

Darby, K. M., Boulanger, R. W., DeJong, J. T. (2017). "Effect of multiple shaking events on cone penetration resistances in saturated sand". Proceedings, 3rd International Conference on Performance-based Design in Earthquake Geotechnical Engineering (PBD-III), Vancouver, BC, Canada, July 16-19.

Dobry, R., and Abdoun, T. (2016). "Research findings on liquefaction triggering in sands during earthquakes". H. Bolton Seed Lecture. Geotechnical and Structural Engineering Congress, ASCE, Phoenix, AZ, February 14-17.

El-Sekelly, W., Abdoun, T., and Dobry, R. (2015). "Liquefaction resistance of a silty sand deposit subjected to preshaking followed by extensive liquefaction". *Journal of Geotechnical and Geoenvironmental Engineering*, 04015101.

El-Sekelly, W., Dobry, R., Abdoun, T., and Steidl, J. H. (2016). "Centrifuge modeling of the effect of preshaking on the liquefaction resistance of silty sand deposits". *Journal of Geotechnical and Geoenvironmental Engineering*, 04016012.

El-Sekelly, W., Abdoun, T., and Dobry, R. (2017). "Effect of sand overconsolidation and extensive liquefaction on K0". Proceedings, Geotechnical Frontiers, ASCE, Orlando, FL, March 12-15.

Finn, W. D. L., Bransby, P. L., and Pickering, D. J. (1970). “Effect of strain history on liquefaction of sand”. *Journal of the Soil Mechanics and Foundations Division*, ASCE, 96(SM6), 1917-934.

Goto, S., and Nishio, S. (1988). “Influence of freeze thaw history on undrained cyclic strength of sandy soils (in Japanese)”.in Proceedings, Symposium on Undrained Cyclic Tests on Soils, Japanese Society for Soil Mechanics and Foundation Engineering,149-54.

Green, R. A., and Terri, G. A. (2005). "Number of equivalent cycles concept for liquefaction evaluations — revisited." *Journal of Geotechnical and Geoenvironmental Engineering,* ASCE, 131. p.477–488.

Ha, I. S., Olson, S. M., Seo, M. W., and Kim, M. M. (2011). “Evaluation of reliquefaction resistance using shaking table tests”. *Soil Dynamics and Earthquake Engineering,* 31(4), 682-691.

Idriss, I. M., and Boulanger, R. W. (2008). *Soil liquefaction during earthquakes,* Earthquake Engineering Research Institute, Oakland, CA.

Ishihara, K. (1996). *Soil Behavior in Earthquake Geotechnics*, The Oxford Engineering Science Series, No. 46.

Kamai, R., and Boulanger, R. W. (2010). “Characterizing localization processes during liquefaction using inverse analyses of instrumentation arrays”. *Meso-Scale Shear Physics in Earthquake and Landslide Mechanics,* Y. H. Hatzor, J. Sulem, and I. Vardoulakis, eds., CRC Press, 219-238.

Kokusho, T., Ito, F., Nagao, Y. & Green, A. R. (2012). “Influence of non/low-plastic fines and associated aging effects on liquefaction resistance”. *Journal of Geotechnical and Geoenvironmental Engineering*, 138(6), 747-756.

Mesri, G., Feng, T. W., and Benak, J. M. (1990). “Postdensification penetration resistance of clean sands”. *Journal of Geotechnical Engineering*, 116(7), 1095-1115.

Mitchell, J. K., and Tseng, D. J. (1990). “Assessment of liquefaction potential by cone penetration resistance”. In Proceedings, H. Bolton Seed Memorial Symposium, Volume 2, J. M. Duncan, ed., BiTech Publishers, Vancouver, B. C., 335-350.

Mulilis, J. P., Seed, H. B., Chan, C. K., Mitchell, J. K., and Arulanandan, K., 1977. Effect of sample preparation on sand liquefaction, J. Geotechnical Eng. Div., ASCE 103(GT2), 91–108.

Oda, M., Kawamoto, K., Suzuki, K., Fujimori, H., and Sato, M. (2001). “Microstructural interpretation on reliquefaction of saturated granular soils under cyclic loading”. *Journal of Geotechnical and Geoenvironmental Engineering,* ASCE 127(5), 416-423.

Parra Bastidas, A. M., Boulanger, R. W., Carey, T. J., DeJong, J. T. (2016). *Ottawa F-65 sand data from Ana Maria Parra Bastidas*. http.//nees.org/resources/13738.

Price, A. B., DeJong, J. T., and Boulanger, R. W. (2017). “Cyclic loading response of silt with multiple loading events”. *Journal of Geotechnical and Geoenvironmental Engineering, in-press*

Pyke, R. M., Chan, C. K., and Seed, H. B., (1974). *Settlement and liquefaction of sands under multi-directional shaking*, Report No. EERC 74-2, Earthquake Engineering Research Center, University of California at Berkeley.

Salgado, R., Mitchell, J. K., and Jamiolkowski, M. (1997). “Cavity expansion and penetration resistance in sands”. *Journal of Geotechnical and Geoenvironmental Engineering*, ASCE 123(4), 344-54.

Seed, H. B., Idriss, I. M., Makdisi, F., and Banerjee, N. (1975). *Representation of irregular stress time histories by equivalent uniform stress series in liquefaction analyses,* Report No. EERC 75-29, Earthquake Engineering Research Center, University of California at Berkeley, CA, October.

Seed, H. B., (1979). "Soil liquefaction and cyclic mobility evaluation for level ground during earthquakes". *Journal of Geotechnical Engineering Division*, ASCE 105(GT2), 201-55.

Seed, H. B., (1983). "Earthquake resistant design of earth dams". In Proceedings, Symposium on Seismic Design of Embankments and Caverns*,* Pennsylvania, ASCE, NY, 41-64.

Singh, S., Seed, H. B., and Chan, C. K., (1982). "Undisturbed sampling of saturated sands by freezing". *Journal of Geotechnical Engineering Division*, ASCE 108(GT2), 247-64.

Skempton, A. W. (1986). "Standard penetration test procedures and the effects in sands of overburden pressure, relative density, particle size, aging and overconsolidation". *Geotechnique*, 36(3), 425-47.

Stewart, D. P., Chen, Y. R., and Kutter, B. L. (1998). "Experience with the use of methylcellulose as a viscous pore fluid in centrifuge models". *Geotechnical Testing Journal*, 21(4), 365-369.

van Ballegooy, S., Malan, P., Lacrosse, V., Jacka, M.E., Cubrinovski, M., Bray, J.D., O'Rourke, T. D., Crawford, S.A., and Cowan, H. (2014) "Assessment of Liquefaction-Induced Land Damage for Residential Christchurch, Earthquake Spectra J., EERI, V. 30(1), 31-55, DOI:10.1193/031813EQS070M.

Ziotopoulou, K., Montgomery, J., Parra Bastidas, A. M., and Morales, B., (2018). "Cyclic strength of Ottawa F-65 sand: laboratory testing and constitutive model calibration". *Proc. International Foundations Congress and Equipment Expo.* ASCE. Orlando, FL.

March 6-10, 2018.

Table 1. CRR, CSR categories and criteria

CRR, CSR category	Criteria
Non-triggering CSR values	Achieve an r_u during shaking <0.95 at both the PPT above and below the CSR depth
High confidence CRR values	1. Achieve an r_u during shaking ≥0.95 at both the PPT above and below the CSR depth 2. The CRR_{15cyc} using the triggering time from the PPT above and the PPT below are within 20% of the average 3. If the triggering time from the PPT above or below is off by half a loading cycle early or late, the CRR_{15cyc} changes by <20% 4. The triggering behavior is the same in both arrays 5. The average CRR_{15cyc} for array 1 and array 2 are within 20% of each other
Medium confidence CRR values	Meet all the criteria for high confidence CRR values except for criterion 1
Low confidence CRR values	Do not meet the high or medium confidence criteria, but reach an r_u≥0.95 at either the PPT above or below in either array 1 or array 2

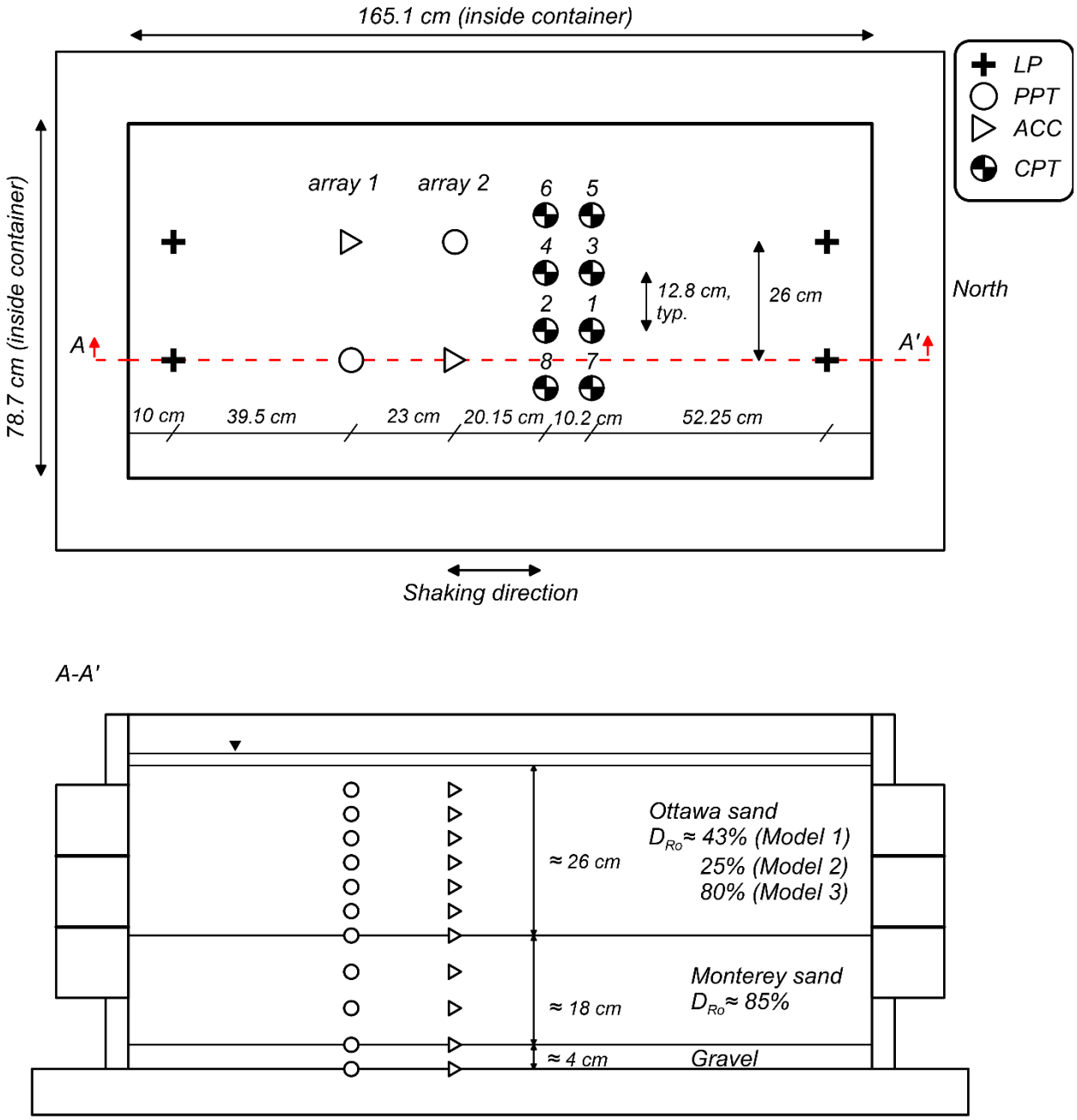

Figure 1. Representative plan view and cross section (model scale).

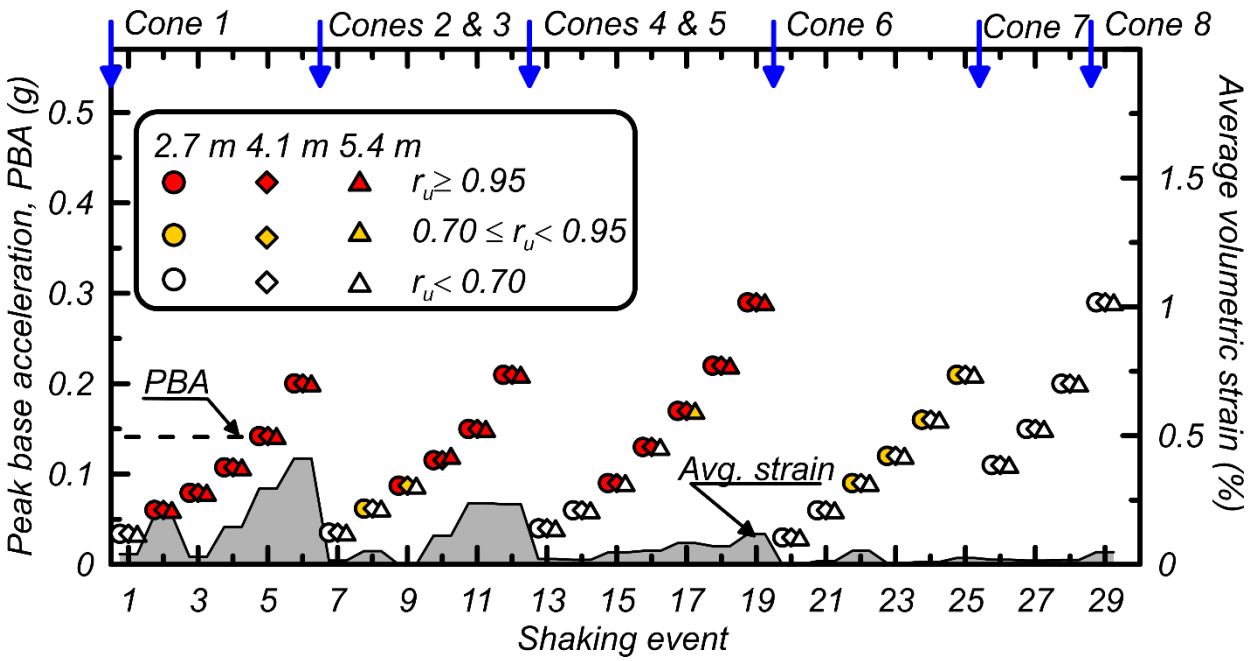

Figure 2. Testing timeline and progression of pore pressure generation and volumetric strains with shaking history in Model 1 (D_{Ro}= 43%).

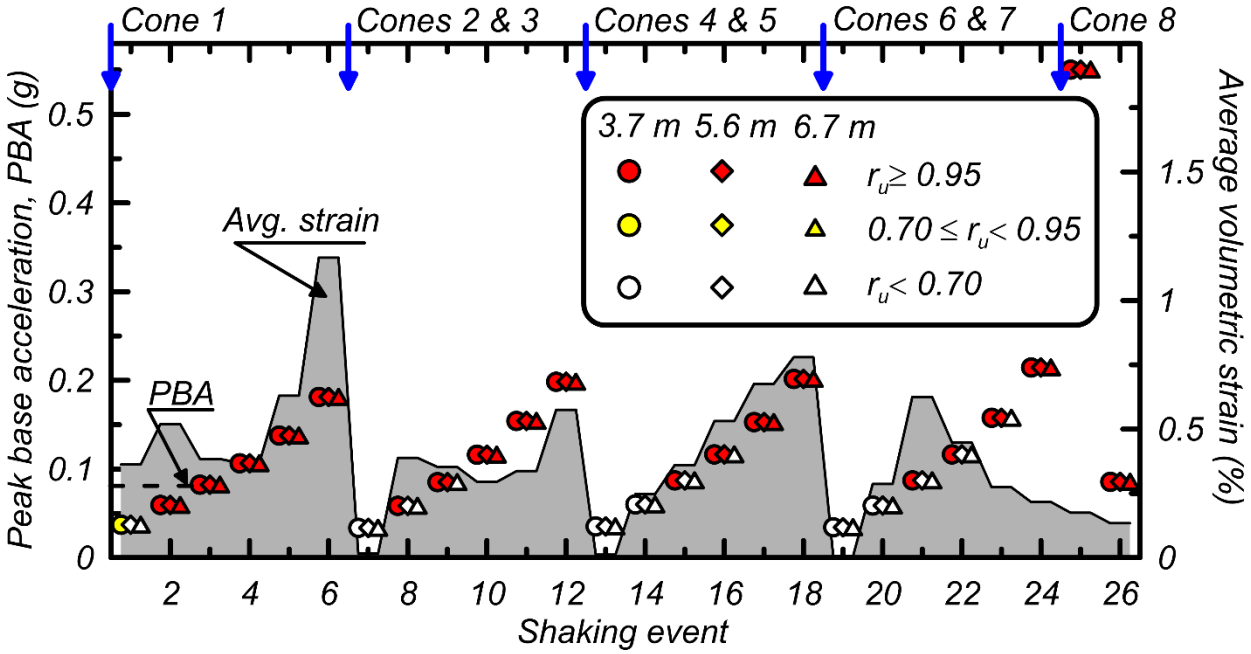

Figure 3. Testing timeline and progression of pore pressure generation and volumetric strains with shaking history for Model 2 (D_{Ro}= 25%).

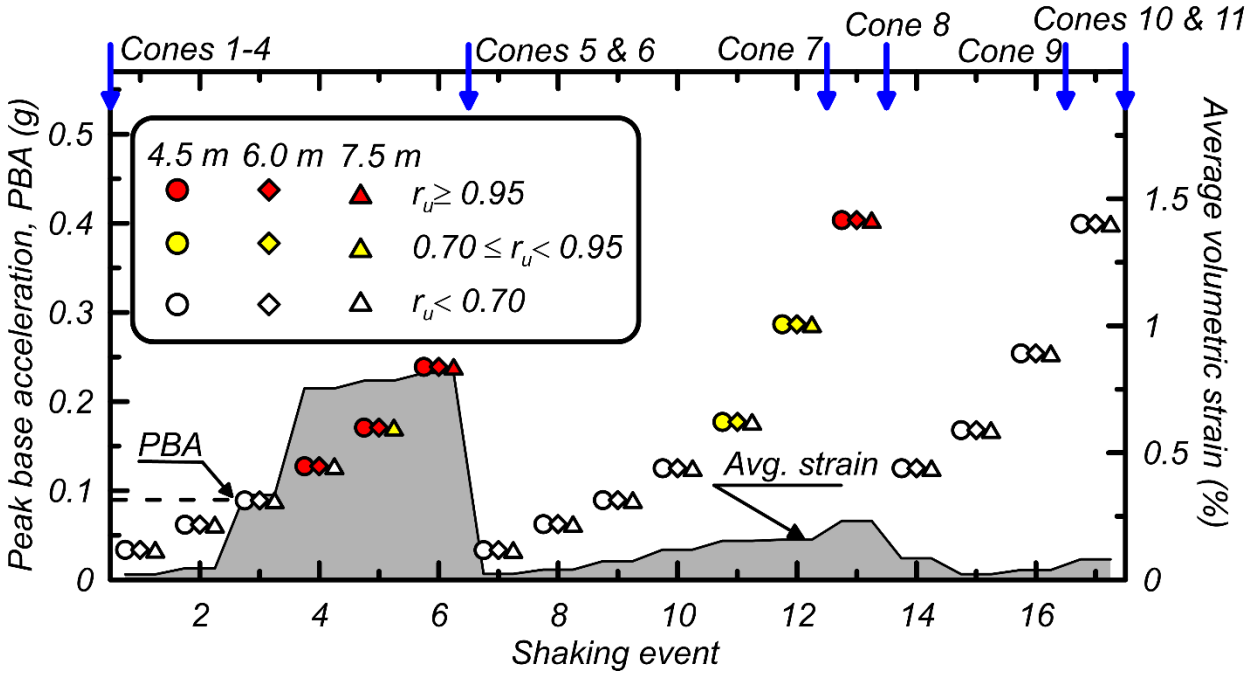

Figure 4. Testing timeline and progression of pore pressure generation and volumetric strains with shaking history for Model 3 (D_{Ro}= 80%).

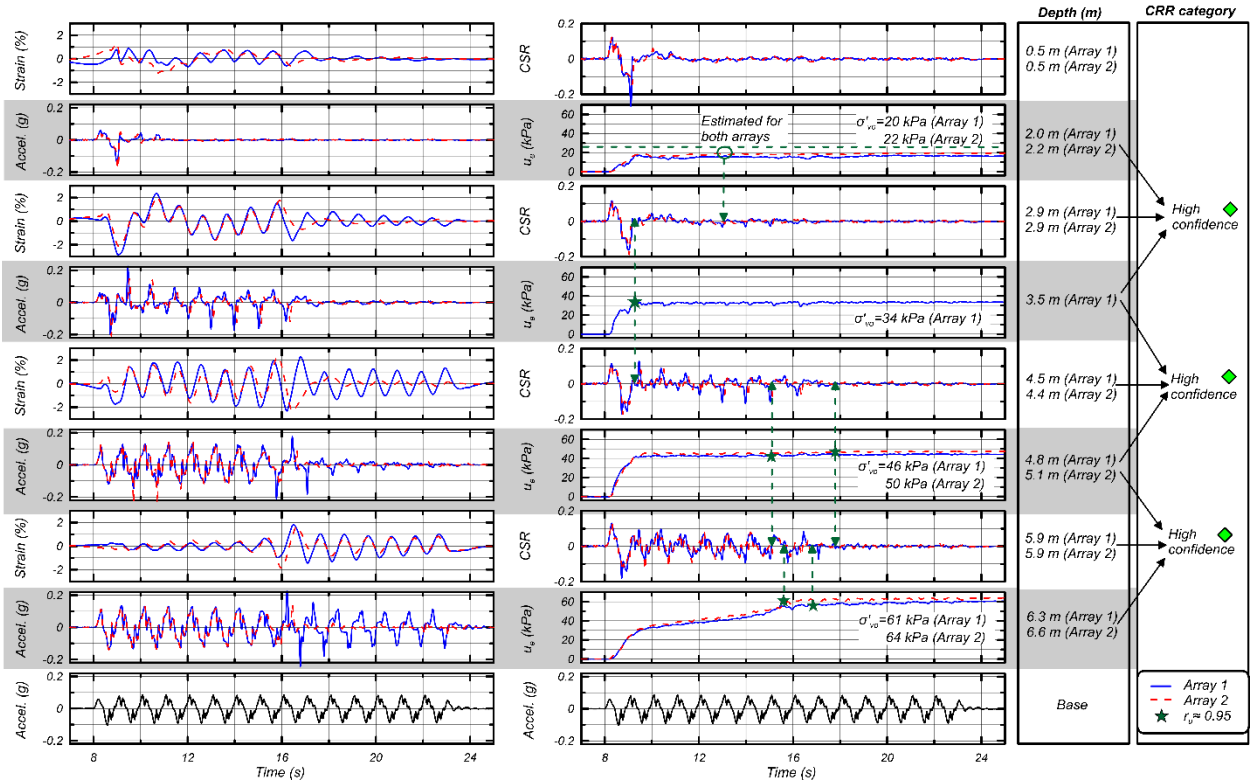

Figure 5. Dynamic responses for Model 1 in shaking event 4 (PBA= 0.11g).

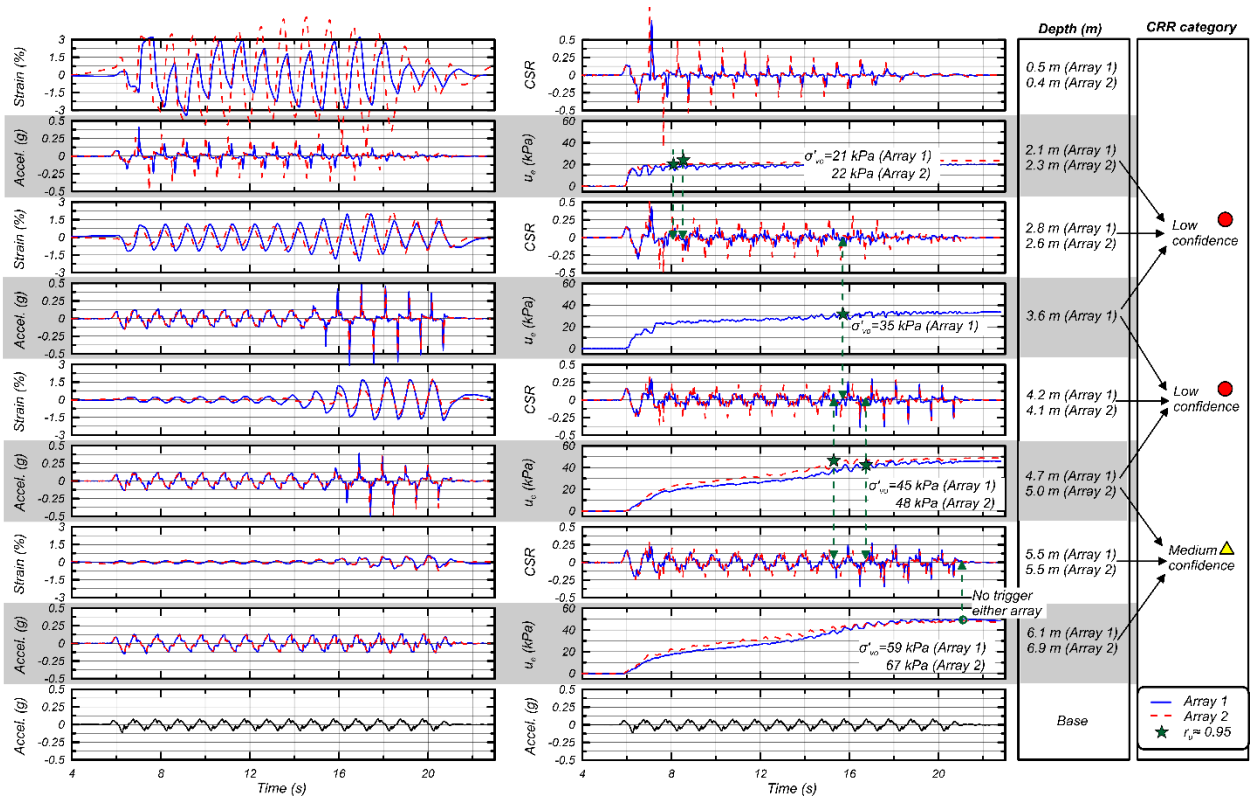

Figure 6. Dynamic responses for Model 1 in shaking event 10 (PBA= 0.12g).

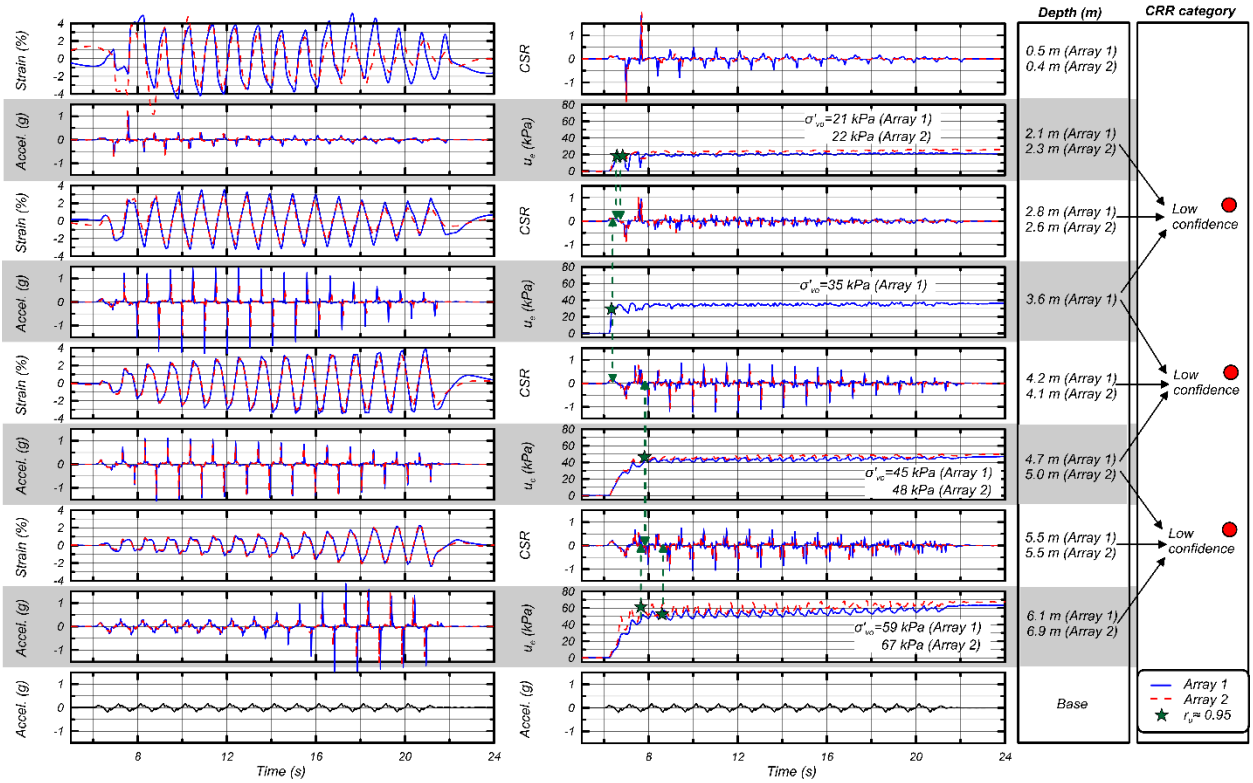

Figure 7. Dynamic responses for Model 1 in shaking event 12 (PBA= 0.21g).

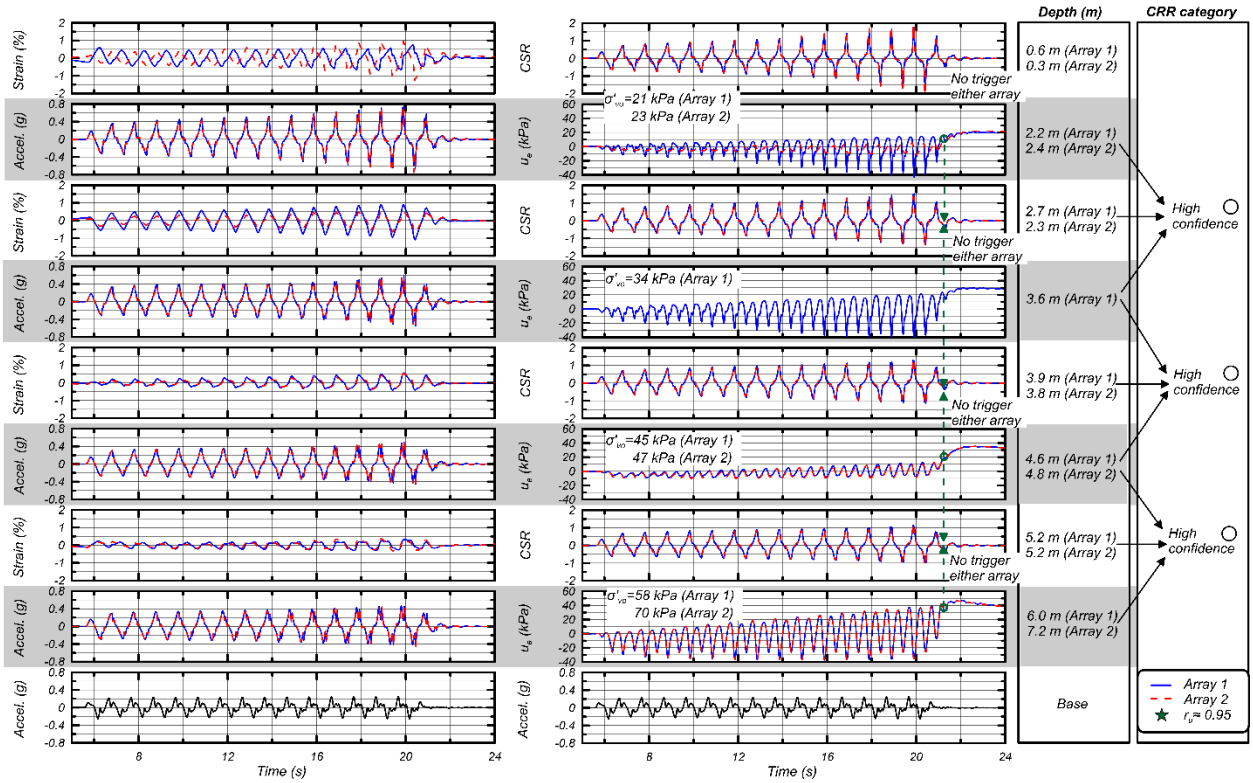

Figure 8. Dynamic responses for Model 1 in shaking event 29 (PBA= 0.29g).

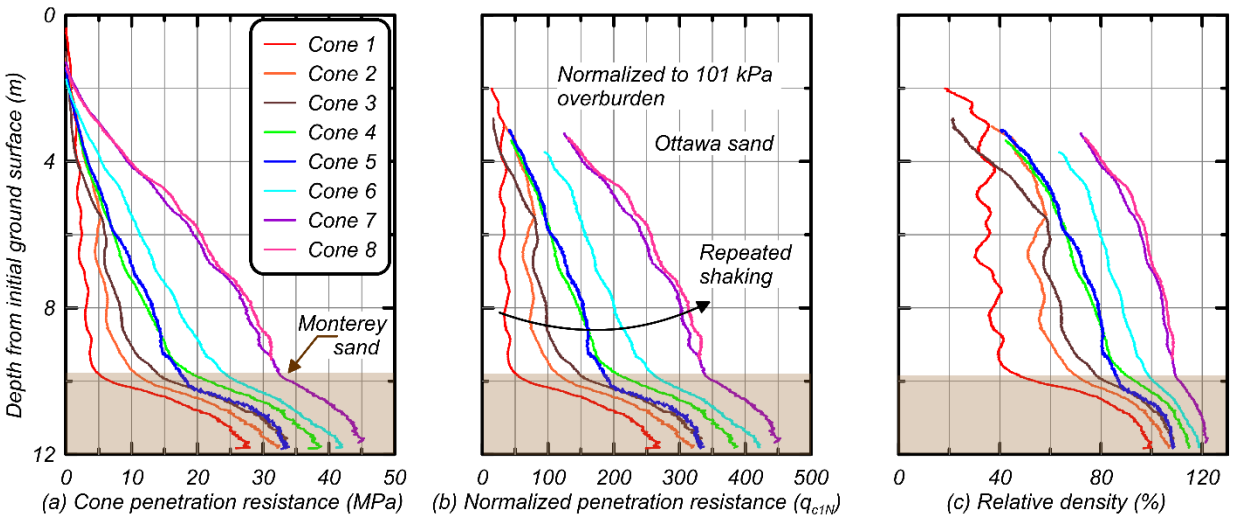

Figure 9. Progression of (a) measured cone penetration resistance, (b) normalized penetration resistance, and (c) estimated relative density, in Model 1 over the sequence of shaking events

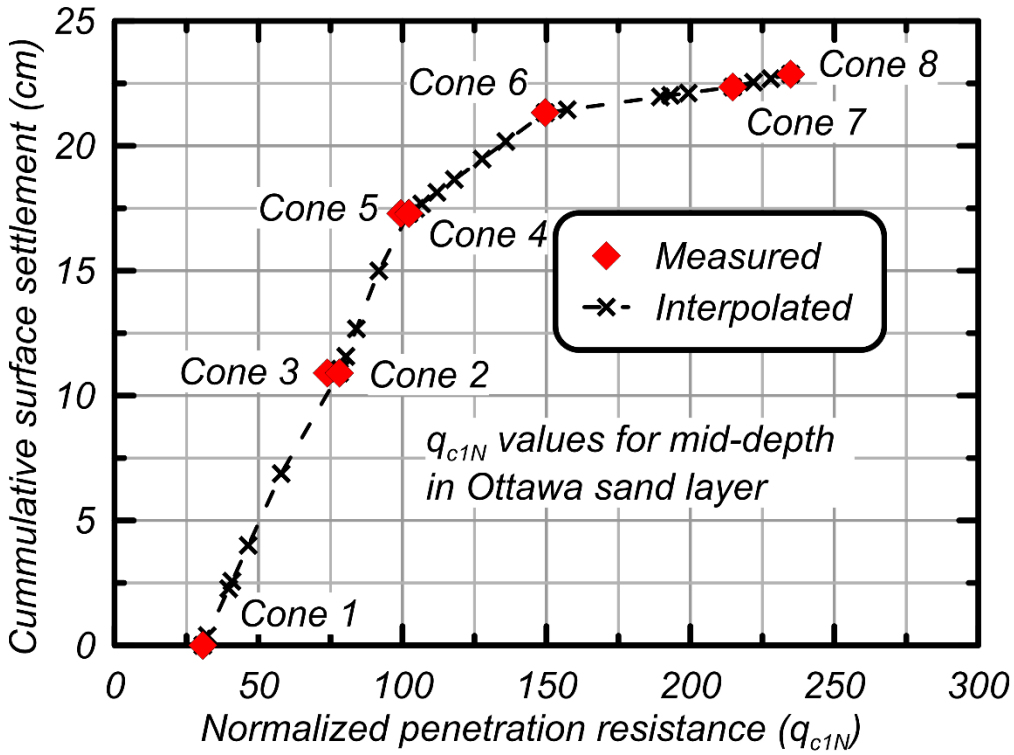

Figure 10. Interpolation of q_{c1N} values between cone pushes for Model 1.

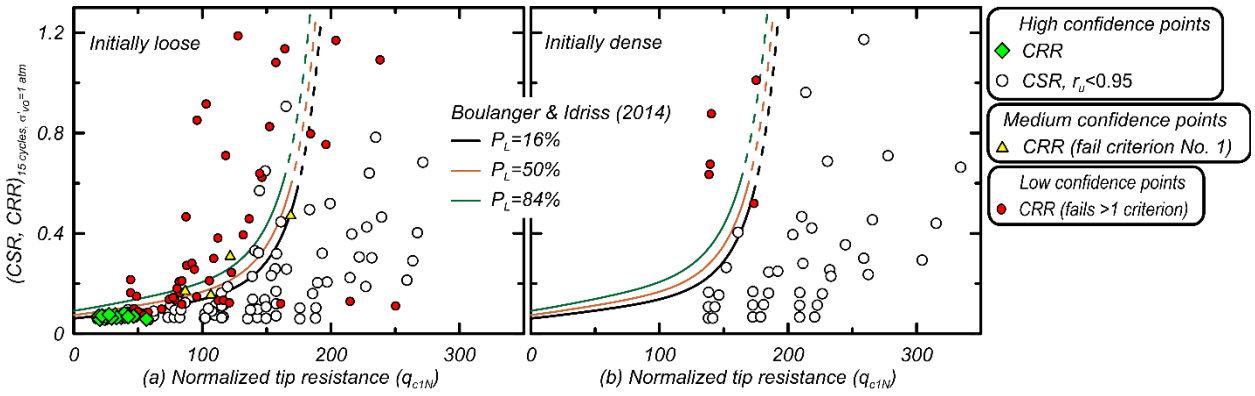

Figure 11. Comparison of $CRR_{15cyc,\sigma'=1}$ – q_{c1N} pairs from the centrifuge tests with the case history based correlation by Boulanger and Idriss (2014): (a) Models 1 and 2, and (b) Model 3.

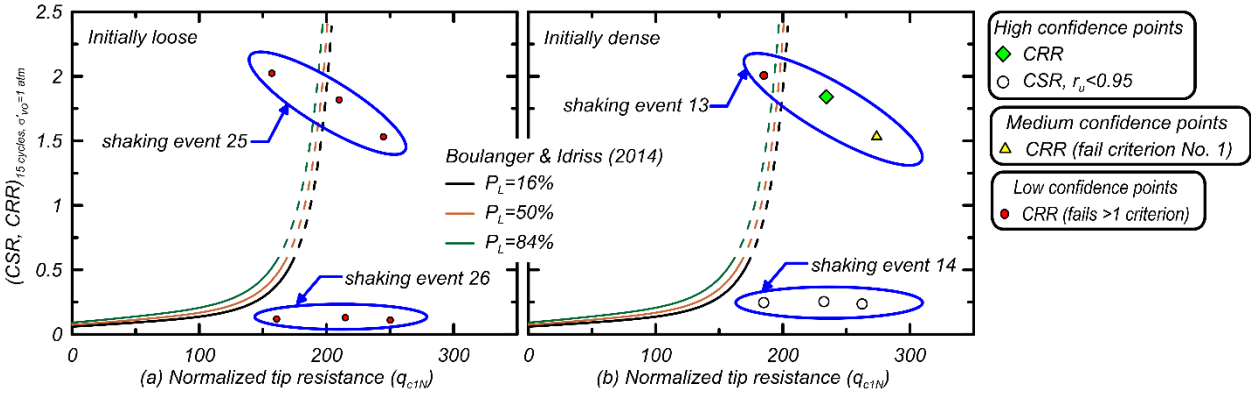

Figure 12. $CRR_{15cyc,\sigma'=1} - q_{c1N}$ pairs for: (a) shaking events 25 and 26 for Model 2, and (b) shaking events 13 and 14 for Model 3.

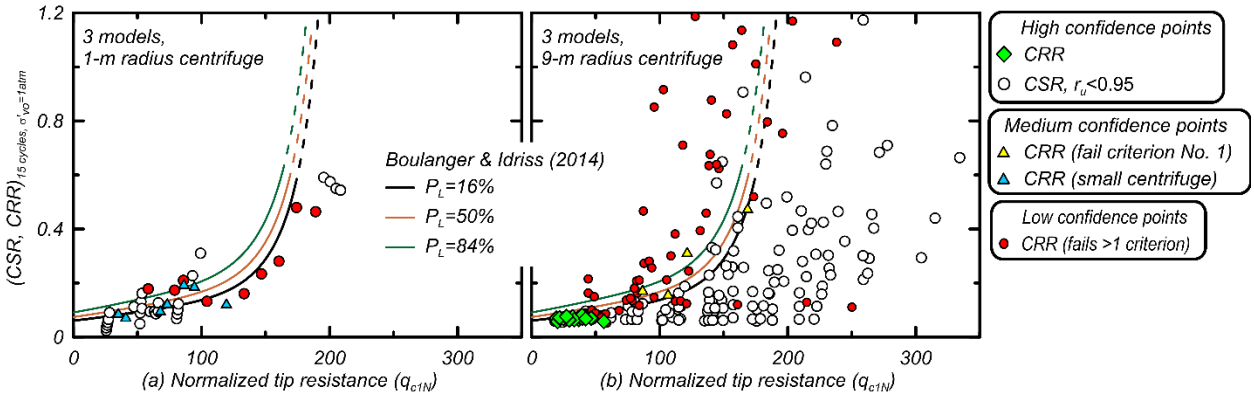

Figure 13. Comparison of $CRR_{15cyc,\sigma'=1} - q_{c1N}$ pairs from (a) three small centrifuge tests and (b) three large centrifuge tests with the case history based correlation by Boulanger and Idriss (2014).

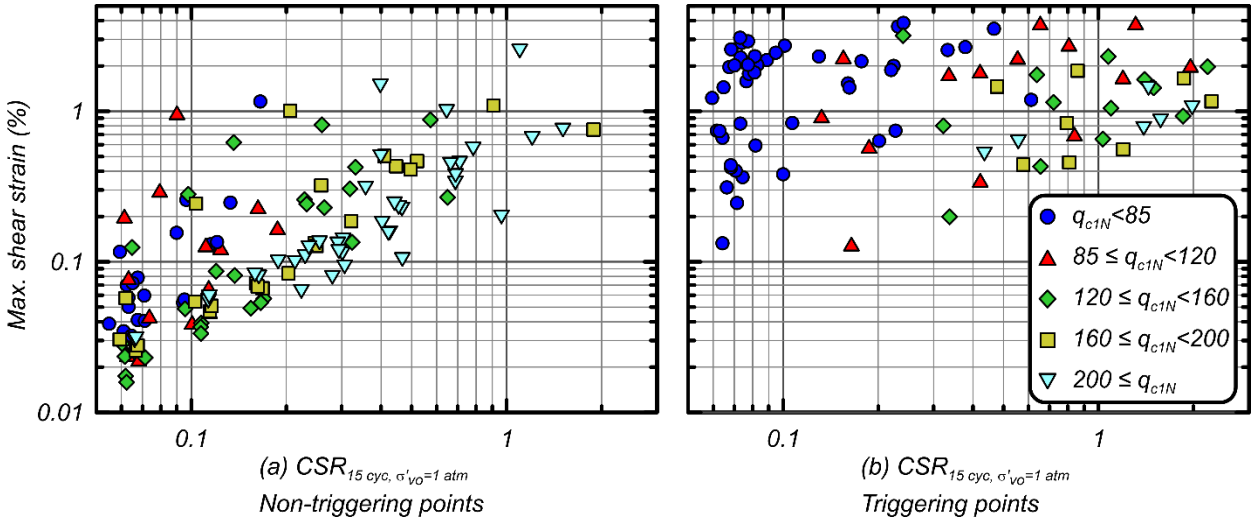

Figure 14. Maximum shear strain versus the equivalent-uniform $CSR_{15cyc,\sigma'=1}$ from the three 9-m radius centrifuge tests for (a) non-triggering points and (b) and triggering points.